Check for updates

LASER & PHOTONICS REVIEWS
www.lpr-journal.org

Computational Adaptive Optics for Fluorescence Microscopy via Sparse Blind Deconvolution

*Runnan Zhang, Heheng Du, Ning Zhou, Zihao Zhou, Hanci Tang, Jiaming Qian, Qian Chen, and Chao Zuo**

Fluorescence microscopy is an indispensable tool for investigating cellular and tissue-level biology, yet its performance is often limited by optical diffraction, aberrations, and noise, resulting in suboptimal imaging quality. Traditional adaptive optics (AO) methods typically rely on additional hardware, such as wavefront sensors, to measure and correct system aberrations, which can be both complex and costly. Here, a computational adaptive optics technique based on sparse blind deconvolution (CAO-SBD) is introduced, which uses a single blurred image to estimate aberrations and perform image deblurring. By incorporating sparse priors of fluorescent specimens with Zernike polynomial-based aberration modeling, CAO-SBD allows for the simultaneous reconstruction of both the aberrated point spread function (PSF) and the sample information, eliminating the need for precise PSF calibration. This method outperforms traditional Richardson-Lucy deconvolution by enhancing robustness to noise and stabilizing the deconvolution process through adaptive PSF correction. Experimental results on bovine pulmonary artery endothelial cells demonstrate that CAO-SBD significantly enhances image resolution and contrast across both wide-field and confocal fluorescence microscopic systems, positioning CAO-SBD as a powerful tool for high-resolution biological imaging with broad applications.

1. Introduction

In the realm of life sciences, light microscopy is acknowledged as an indispensable tool for probing the complexities of the microscopic universe, thus playing a crucial role in the exploration of subcellular dynamics, neuroscientific research, oncological diagnostics, and a multitude of other fields.[1,2] The historical evolution of microscopes has been characterized by an unceasing quest for enhanced imaging capabilities, with a reliance on sophisticated optical systems. This advancement has been instrumental in revealing the minute details within cellular structures and capturing the intricate dynamics of life processes. However, the presence of optical aberrations poses a significant challenge to achieving perfect imaging.[3–6] In light microscopy, the performance of which is fundamentally constrained by the design parameters of the optical systems.[7,8] The achievement of high-quality imaging resolution is dependent on the precise alignment of meticulously polished lenses, while aberrations potentially arise from defects and misalignments of the illumination or detection optical components.[9,10] Therefore, a profound understanding of these aberrations and the development of effective correction methodologies are essential for facilitating high-resolution imaging. Adaptive optics (AO) is a commonly used method to enhance the imaging performance of microscopes.

Traditional AO, which usually employs a deformable mirror (DM) array or spatial light modulator (SLM) to correct wavefront aberrations actively, enables high-resolution imaging by directing light rays from a single source to a common focal point on the sensor at varying angles.[11–13] It was initially developed to mitigate the image degradation caused by atmospheric turbulence in ground-based telescopes, playing a pivotal role in the groundbreaking research that led to the Nobel Prize-awarded discovery of a massive, dense object at the center of our galaxy.[14–17] Subsequently, AO was integrated into microscopy to correct for aberrations arising from sample refractive index inhomogeneities, component defects, microscopy misalignments, among others, thereby enhancing imaging quality. Wavefront sensors, such as the Shack-Hartmann sensor, utilize a grid of lenses to segment the incoming wavefront and direct the light from each section toward a detector. By determining the local tilt of the wavefront in each segment, the wavefront is reconstructed.[18–25] Light field imaging, with a microlens array inserted into the optical path, recording the light traveling along ray bundles inside the cam-

R. Zhang, H. Du, N. Zhou, Z. Zhou, H. Tang, J. Qian, C. Zuo
Smart Computational Imaging Laboratory (SCILab), School of Electronic and Optical Engineering
Nanjing University of Science and Technology
Nanjing, Jiangsu 210094, China
E-mail: zuochao@njust.edu.cn

R. Zhang, H. Du, N. Zhou, Z. Zhou, H. Tang, J. Qian, Q. Chen, C. Zuo
Jiangsu Key Laboratory of Spectral Imaging & Intelligent Sense
Nanjing University of Science and Technology
Nanjing, Jiangsu 210094, China

R. Zhang, H. Du, N. Zhou, Z. Zhou, H. Tang, J. Qian, C. Zuo
Smart Computational Imaging Research Institute (SCIRI) of Nanjing University of Science and Technology
Nanjing, Jiangsu 210019, China

The ORCID identification number(s) for the author(s) of this article can be found under https://doi.org/10.1002/lpor.202500032

DOI: 10.1002/lpor.202500032

 © 2025 Wiley-VCH GmbH

era, which facilitates the computation of photographs with reduced lens aberrations.[26–31] Wavefront correction equipment, such as DM or SLM, achieves active aberration correction by artificially loading phases for compensation.[11,12] However, the integration of such hardware with various microscope optical paths is challenging, thus limiting its universal applicability. To overcome this, techniques such as Fourier ptychographic microscopy and differential phase contrast microscopy, use phase retrieval algorithms to optimize the signals received by photoelectric detectors to correct the wavefront.[32–38] Leveraging inherent data redundancy, they simultaneously recover the complex field of the specimens and the spatially varying aberrations of systems, and perform measurements after correction, enabling the reconstruction of high-quality images without relying on additional aberration compensation hardware, thereby achieving high-resolution imaging.

However, these methods typically require the acquisition of multiple images or additional hardware. To overcome this, we demonstrated a computational adaptive optics (CAO) algorithm through blind deconvolution, which uses computational algorithms to correct imaging distortions without the need for additional hardware. Blind deconvolution is a technique that estimates both the aberrated point spread function (PSF) and the original object from a single blurred observation.[39–45] The majority of fluorescent microscopy systems operate as a linear system with spatially invariant PSF, wherein the blurred image on the imaging plane is generated by the convolution of the PSF with the original object.[46]

To obtain a clear image, various deconvolution approaches have been proposed to mitigate image degradation. Among these, the Richardson-Lucy deconvolution (RLD) algorithm,[47,48] which computes maximum likelihood estimation (MLE) adapted to Poisson statistics, is well-known for its ability to restore images degraded by Poisson-distributed noise, making it effective in applications such as fluorescence microscopy. However, aberrations arise from misalignments within the imaging system, which will cause aberrations, leading to discrepancies between the actual PSF and the PSF derived from theoretical calculations. These discrepancies, in turn, result in terrible deconvolution results. In such cases, blind deconvolution is an appropriate solution to obtain a sharper image, wherein one tries to recover the original object in the absence of any system knowledge and adaptively adjusts the PSF based on the system's aberrations. However, blind deconvolution is inherently challenging due to its ill-posed nature,[49] which makes it unstable and highly sensitive to the PSF estimation, therefore it is difficult to get approximate solutions. The best that can be done is to employ regularizers to find an approximate solution. Sparsity, a concept that has been effectively utilized in the field, serves as a suitable criterion for identifying appropriate regularizers, particularly in fluorescent imaging.[50] The majority of the fluorescence intensity in the specimens is concentrated in a few distinct regions, while the rest of the regions exhibit negligible or zero.

In this paper, we proposed a new computational adaptive optics method on the basis of blind deconvolution, termed CAO-SBD, which utilizes the prior knowledge of natural image statistics, typically the sparsity of their derivative distributions for fluorescent imaging, to identify the PSF kernel that maximizes the maximum a posteriori (MAP). We further refine the estimated PSF with Zernike polynomial-based aberration modeling. To achieve aberration correction with a single image, we incorporate prior knowledge of common aberrations into our reconstruction process, choosing Zernike polynomials[51] as an appropriate basis for expressing pupil aberrations, which simplifies the solution space by reducing the degrees of freedom from a 2D matrix to a minimal set of coefficients corresponding to the Zernike modes, thus benefiting reconstruction using a single raw image.[52] In order to validate the performance of our method, we conducted experiments on bovine pulmonary artery endothelial cells (BPAEC) with labeled mitochondria, F-actin, and nuclei. Our proposed CAO-SBD method is capable of retrieving the aberrations of the imaging system through only a single image and is robust to noise, thus outperforming the traditional RLD method in both wide-field fluorescence and confocal microscopy, revealing our method is a promising tool for broad applicability and diverse applications.

2. Methods

2.1. Imaging Formation and Algorithm Framework

Fluorescence microscopy employed the phenomena of fluorescence and phosphorescence to investigate the characteristics of organic or inorganic materials, offering an alternative or complementary method to traditional techniques that rely on reflection or absorption. However, due to the wave nature of light, a point in the object space, when perfectly transferred to the image space, forms an Airy disk due to diffraction.[53] Of the diffracted light produced by an object, only a portion incident through the pupil aperture, leading to the loss of high-frequency light information with a larger wave vector angle, thus creating a diffraction spot of a certain size on the imaging plane. Owing to the incoherent nature of the emitted fluorescence light, most fluorescence microscopy could be described as a linear space-invariant system, where the PSF of the imaging system convolved with the object, resulting in image distortion on the image plane. On the other hand, imaging systems were inevitably subject to Poisson noise due to photon-limited detection or extrinsic noise such as image sensors. As shown in **Figure 1a**, the imaging process can be expressed analytically as:

$$g(x,y) = f(x,y) \otimes h(x,y) + n(x,y) \tag{1}$$

where $g(x,y)$ is the distortion image, $f(x,y)$ is the original object, $h(x,y)$ is the PSF of imaging system, $n(x,y)$ is the noise, and $\otimes$ is the convolution operator. For a wide-field fluorescence microscope, the PSF can be represented as the auto-correlation of the pupil function:

$$h(x,y) = \mathscr{F}^{-1}[P(\xi,\eta) \star P^{*}(\xi,\eta)] \tag{2}$$

where (ξ,η) is the spatial frequency variables corresponds to (x,y), $P(\xi,\eta)$ is the pupil function, * is the complex conjugate operator, and $\star$ denotes the autocorrelation operation. Typically, the pupil P is a circular function with its radius determined by the

© 2025 Wiley-VCH GmbH

18638899, 0, Downloaded from https://onlinelibrary.wiley.com/doi/10.1002/lpor.202500032 by Nanjing University Of Science, Wiley Online Library on [09/05/2025]. See the Terms and Conditions (https://onlinelibrary.wiley.com/terms-and-conditions) on Wiley Online Library for rules of use; OA articles are governed by the applicable Creative Commons License

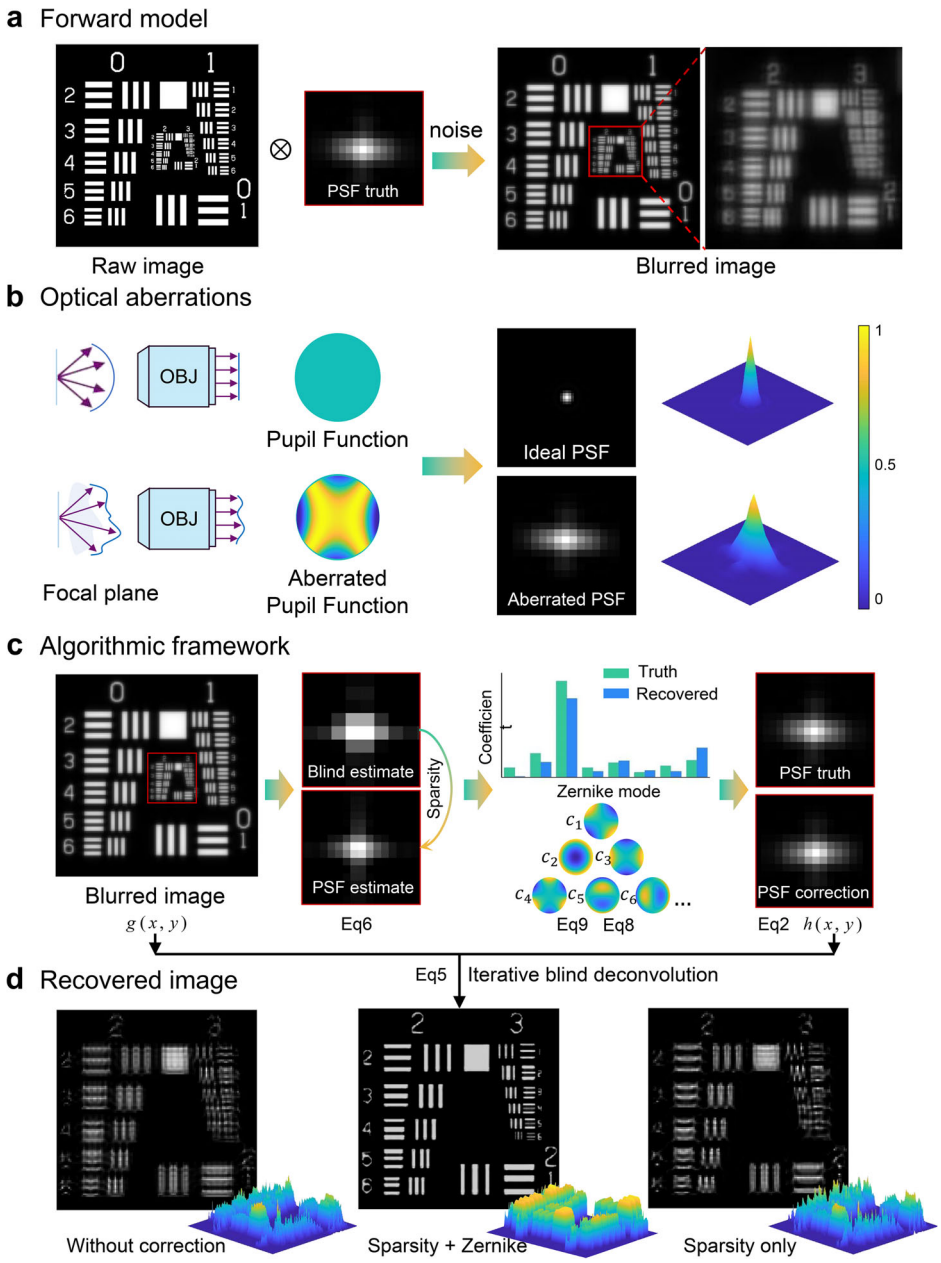

Figure 1. Schematic diagram of the proposed CAO-SBD method. a) The forward model of an ideal imaging system. b) Aberration effect in the optical system. c) Algorithm framework: estimating the system's PSF from a single blurred image under sparse priors, and refining the estimated PSF with Zernike constraints. d) The restoration of the blurred image, where combining sparsity priori and Zernike constraints can achieve optimal performance.

numerical aperture (NA) of the objective lens, and wavelength λ:

$$P(\xi,\eta)=\begin{cases}1, & if \quad \left|\sqrt{(\xi^2+\eta^2)}\right| \leqslant \rho_p \\ 0, & if \quad \left|\sqrt{(\xi^2+\eta^2)}\right| > \rho_p\end{cases} \tag{3}$$

where $\rho_p = NA/\lambda$ is the cut-off frequency of the pupil function.

Image deblurring algorithms could enhance image contrast by accurately estimating the PSF. Wiener deconvolution[54] and Richardson-Lucy deconvolution[47,48] were typically algorithms for image deblurring. However, the results depend on an extremely precise PSF. The use of theoretically derived PSF was not always applicable because differences always exist between the theoretical and the practical PSF.[55] The calibration of the PSF in fluorescence microscopy was commonly achieved by imaging small fluorescent beads. This process could be tedious and esoteric, involving the management of several challenges: significant noise due to low light efficiency conditions, the accurate empirical matching of the refractive index of the immersion oil, the photobleaching of beads, the isolation and identification of indi-

© 2025 Wiley-VCH GmbH

18638899, 0, Downloaded from https://onlinelibrary.wiley.com/doi/10.1002/lpor.202500032 by Nanjing University Of Science, Wiley Online Library on [09/05/2025]. See the Terms and Conditions (https://onlinelibrary.wiley.com/terms-and-conditions) on Wiley Online Library for rules of use; OA articles are governed by the applicable Creative Commons License

vidual beads, and the erroneous smearing of the PSF caused by bead size.

As depicted in Figure 1b, in the practical imaging system, the pupil function was subject to optical aberrations originating from the imperfect alignment in the imaging system. In the presence of aberrations, the wavefront distortion lead to phase variations across the pupil, introducing a phase component to the pupil function.

$$P'(\xi,\eta) = P(\xi,\eta)e^{i\varphi(\xi,\eta)} \tag{4}$$

This phase component, carried by the pupil function, will further affect the PSF and result in a worse performance of the imaging system. Adaptive optics methods could compensate for the aberrations in imaging systems but often require complex optical components. The term "blind deconvolution" refers to the process of deconvolving a corrupted signal without the need for a prior determination of the PSF or calibration. In the blind deconvolution approach, both the object image and the PSF were presumed to be unknown, and they were estimated iteratively. The algorithm employed the standard MLE algorithm (a statistical method where the parameter values were chosen to maximize the likelihood function), together with a PSF estimation for each iteration. The process of blind deconvolution could be represented as:

$$\begin{aligned} f^{k+1}(x,y) &= f^k(x,y)\left\{\left[\frac{g(x,y)}{f^k(x,y)*h^k(x,y)}\right] * h^k(-x,-y)\right\} \\ h^{k+1}(x,y) &= h^k(x,y)\left\{\left[\frac{g(x,y)}{f^k(x,y)*h^k(x,y)}\right] * f^k(-x,-y)\right\} \end{aligned} \tag{5}$$

Although band-limited and non-negative constraints were often performed on PSF estimation, the conventional blind deconvolution algorithm often suffers from slow convergence and unstable estimations. Applying initial guess smoothing and regularization functions can enhance convergence speed and accuracy. Here, a blind deconvolution solution was proposed, the algorithm flowchart of which is shown in Figure 1c.

For the blind deconvolution problem, due to the existence of many pairs $(f(x,y), h(x,y))$ that could explain the observed blurred image $g(x,y)$, the feasible solutions were not only unstable but also non-unique, making the recovery process a highly ill-posed problem. Unlike the standard MLE algorithm as depicted in Equation (5), the MAP estimator (estimation extends MLE by incorporating prior beliefs about the parameters) of the blur kernel $h(x,y)$ was approximated using a sparse derivative prior. Although a simultaneous MAP estimation of both image $f(x,y)$ and kernel $h(x,y)$ was ill-posed, estimating the kernel $h(x,y)$ alone was more well-conditioned since the number of parameters to be estimated was relatively small compared to the number of pixels in the measured 2D matrix (See Section S1, Supporting Information).

As shown in Figure 1c, effective yet realistic constraints were applied to the PSF solution. Leveraging prior knowledge from natural image statistics, particularly the sparsity of the derivative distribution in fluorescence imaging, served as an appropriate criterion for determining the suitable regularizer and for identifying the PSF kernel that maximizes the posterior probability. In this paper, the sparse prior was represented as a mixture of MOG (See Section S2, Supporting Information). A sparsity prior was utilized in the estimation of the blur kernel and enforce non-negativity for all its terms. The optimal PSF kernel were determined for a given image by considering the covariance surrounding the image estimate, rather than just the mean of the image estimate itself. Specifically, the blur kernel from a single blurred image was estimated by finding the PSF kernel that minimizes Equation (6):

$$\hat{h}(x,y) = \arg\min_{h(x,y)}[||f(x,y)\otimes h(x,y) - g(x,y)||^2] \tag{6}$$

The minimization of Equation (6) could be readily accomplished by solving the quadratic programming problem. It had been derived that minimizing Equation (6) through the solution of the quadratic programming problem is equivalent to minimizing Equation (7) (See Section S2, Supporting Information):

$$\hat{h}(x,y) = \arg\min_{h(x,y)} \frac{1}{2}h^T(x,y)A_h{}^T h(x,y) - b_h{}^T h(x,y) \tag{7}$$

where A_h represents the covariance around the image estimate, and b_h indicates the correlation with blurred image. To further enhance the accuracy of the estimated kernel $h(x,y)$, the aberrations of the imaging system were taken into account. The aberration estimation refined the PSF kernel derived from Equation (7) by fitting it with Zernike polynomials, which were chosen as the appropriate basis to express the pupil aberrations:

$$P_c(\xi,\eta) = P(\xi,\eta)\prod_{m=0}^{M} e^{ic_m Z_m} \tag{8}$$

where M represents the total number of Zernike modes, and c_m denotes the coefficients of each orthogonal Zernike mode Z_m. Specifically, the aberration estimation initializes the Zernike coefficient matrix $\mathbf{c} = [c_1, c_2 \ldots, c_m]$ to 0, fits the PSF kernel derived from Equation (7) using Zernike polynomials, and employed the method of least squares to perform the aberration estimation process. The goal is to solve for the coefficient matrix $\mathbf{c}$ that minimizes Equation (9):

$$\mathbf{c} = \arg\min_{\mathbf{c}} \{\mathcal{F}^{-1}[P_c(\xi,\eta) \star P_c(\xi,\eta)] - h(x,y)\}^2 \tag{9}$$

The Zernike aberration coefficient matrix $\mathbf{c}$ obtained by solving Equation (9), was substituted into Equation (8) to reconstruct the aberration-corrected pupil function. Subsequently, the initial PSF is computed via the autocorrelation of the pupil function as defined in Equation (2). Using as the initial estimate PSF, the alternating optimization framework in Equation (5) was employed to perform iterative deconvolution, achieving clear restoration of blurred images.

Therefore, the complexity of solving for the kernel was diminished, as the solution's dimensionality was condensed from a 2D matrix to a compact set of coefficients that correspond to Zernike modes, facilitating the PSF estimation from a single image. As illustrated in Figure 1d, the comparison results for RLD (without PSF estimation), blind deconvolution with only sparsity priors, and blind deconvolution with both sparsity priors and Zernike fitting (CAO-SBD method) were clear and straightforward. For

© 2025 Wiley-VCH GmbH

18638899, 0, Downloaded from https://onlinelibrary.wiley.com/doi/10.1002/lpor.202500032 by Nanjing University Of Science, Wiley Online Library on [09/05/2025]. See the Terms and Conditions (https://onlinelibrary.wiley.com/terms-and-conditions) on Wiley Online Library for rules of use; OA articles are governed by the applicable Creative Commons License

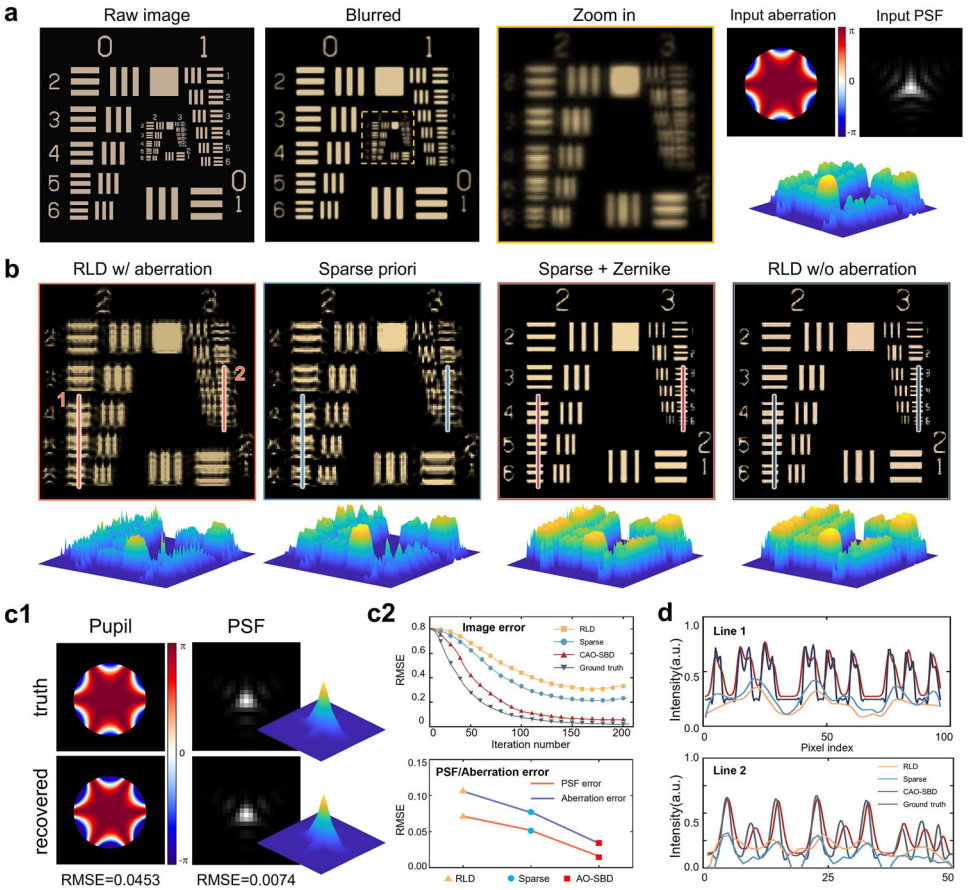

Figure 2. Simulation results on a USAS target. a) The USAF target and the blurred one considering the impact of aberrations. b) Comparison of image reconstruction results under different PSFs. c1) Comparison of simulated pupil aberrations, PSF, and the estimates obtained from our blind deconvolution method. c2) Comparison of the estimated pupil aberrations, PSF by different methods, and the corresponding deconvolution reconstruction results. d) Line plots of b) to compare imaging resolution and contrast.

the restoration of blurred images, optimal performance could be achieved by combining both sparsity priors and Zernike fitting.

2.2. Simulation and Analysis

To quantitatively evaluate the performance of the proposed blind deconvolution method, a simulation was conducted on a USAF resolution target. The simulation parameters were chosen to match the wide-field fluorescence microscope experimental setup described in the subsequent wide-field fluorescent experiment, specifically a 40×/0.6NA objective lens, a central wavelength of 520 nm, and a spatial sampling interval of 162.5 nm. The simulation results were demonstrated in **Figure 2**, aiming to comprehensively validate and demonstrate the applicability and effectiveness of the proposed method, proving that the blind deconvolution scheme could accurately characterize aberrations and restore the original object. Figure 2a shows the original image of the USAF resolution target and the PSF blur result under the influence of aberrations. The "Blurred" represents the blurred image, and "Zoom-in" was the enlarged region of interest, showing the simulated aberrations and the distorted PSF affected by them, with the simulated aberrations constructed as a sum of several Zernike polynomials.

As shown in Figure 2b, the deconvolution results were compared under different PSFs. The reconstruction results using the traditional RLD algorithm (with aberration but using ideal PSF for RLD), blind deconvolution with only sparse priors added, and CAO-SBD method were presented, and compared with the image reconstruction using traditional RLD algorithm (without aberration and the PSF was ideal), respectively. To facilitate subsequent discussions and maintain clarity throughout the manuscript, the traditional RLD algorithm (with aberration but using ideal PSF for RLD) was denoted as RLD and the traditional RLD algorithm (without aberration and the PSF is ideal) as ground truth. The intensity plots after reconstruction in the Zoom-in region were also shown more intuitively to observe the changes in intensity. The results indicate that when aberrations were presented, the RLD reconstruction results were suboptimal due to the difference between the theoretical PSF and the actual PSF. The quality of the deconvolution reconstruction was improved by introducing prior knowledge, especially the sparsity of the derivative distribution in fluorescence imaging, but there was still room for improvement in image resolution. Further refinement of the estimated PSF

© 2025 Wiley-VCH GmbH

18638899, 0, Downloaded from https://onlinelibrary.wiley.com/doi/10.1002/lpor.202500032 by Nanjing University Of Science, Wiley Online Library on [09/05/2025]. See the Terms and Conditions (https://onlinelibrary.wiley.com/terms-and-conditions) on Wiley Online Library for rules of use; OA articles are governed by the applicable Creative Commons License

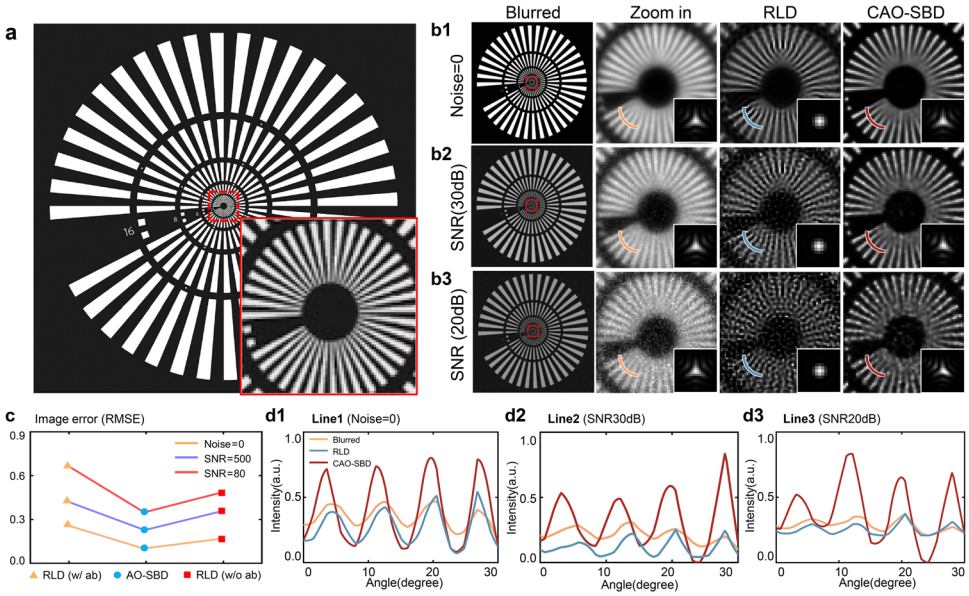

Figure 3. Noise robustness analysis. a) Raw image. b) Blurred images obtained at different SNRs(dB), and a comparison of the restoration effects between traditional RLD and our blind deconvolution method. c) RMSE error curves of image reconstruction results for several methods at different SNRs. d1–d3) Contour profiles of the selected arc area in (b) at different SNRs, comparing noise resistance effects.

through aberration estimation using Zernike polynomials, i.e., deconvolution with sparse priors combined with Zernike constraints (according to Equation (8)), results in reconstructed images that exhibit more pronounced details and sharper edges, almost identical to the reconstruction results under the ideal condition.

Figure 2c1 shows the simulated pupil aberrations and PSF disturbed by aberrations, as well as the results estimated by blind deconvolution, with the root mean square error (RMSE) between the pupil aberration and PSF estimated and the true values being as low as 0.0453 and 0.0074, respectively. Figure 2c2 presents the error curves of image deconvolution reconstruction results under different conditions corresponding to Figure 2b, as well as the RMSE between the pupil aberration and PSF estimates and the true values, demonstrating that sparse priors enhance the accuracy of PSF estimation, and the combination of sparse priors with Zernike constraints further enhance estimation accuracy.

Figure 2d provides profiles of different reconstructed images as shown in Figure 2b, further demonstrating the comparison between the ideal reconstructed image, the traditional RLD method, and the blind deconvolution method. The results showed that under the combination of sparse priors and Zernike constraints, the pixel values at fine structures exhibit significant peak and valley characteristics, with the image restoration results being closest to the true values; in contrast, the pixel value changes in other methods were relatively flat, approximately linear, indicating that the best performance can be achieved by combining image gradient sparsity and Zernike constraints. As shown in Figure 2, the proposed blind deconvolution method could efficiently estimate both PSF and pupil aberration, and the deconvolution result was comparable to the ground truth.

3. Results

3.1. Robustness Against Noise Sensitivity of CAO-SBD Method

In the previous sections, we have constructed a forward model of an ideal imaging system and proposed a CAO-SBD method. However, in the derivation process and simulations, we did not consider the impact of noise on image quality. As depicted in Equation (1), noise is one of the significant factors that destroy image quality in practical applications. An important drawback of the traditional RLD method, however, is that it amplifies noise after a few iterations.

Another advantage of the CAO-SBD method is that it can suppress the unavoidable noise in the image. We believe that the sparsity of fluorescence images and the Zernike-constrained PSF are general characteristics of fluorescence microscopy that can be used as prior knowledge to suppress noise and facilitate the extraction of high-frequency information. As shown in **Figure 3**, we assessed the noise resistance level of the proposed blind deconvolution method, testing the restoration effect of blind deconvolution on blurred images at different noise levels and comparing it with the traditional RLD algorithm with and without aberration. The choice of simulation parameters matches the wide-field fluorescence microscope experimental setup described in the following wide-field fluorescent experiment, specifically a 40×/0.6NA objective lens, a central wavelength of 520 nm, and a spatial sampling interval of 162.5 nm.

Figure 3a shows the original image without PSF blurring and noise interference, with the red square area highlighting the central details. We applied different levels of noise to the original image, as shown in Figure 3b, which displays blurred images at noise levels of no noise, a signal-to-noise ratio (SNR) of 30dB and an SNR of 20dB. The zoomed-in region compares the differences

© 2025 Wiley-VCH GmbH

18638899, 0, Downloaded from https://onlinelibrary.wiley.com/doi/10.1002/lpor.202500032 by Nanjing University Of Science, Wiley Online Library on [09/05/2025]. See the Terms and Conditions (https://onlinelibrary.wiley.com/terms-and-conditions) on Wiley Online Library for rules of use; OA articles are governed by the applicable Creative Commons License

in fine structures of the blurred images and the reconstruction results between the traditional RLD method and our CAO-SBD method. The estimated PSF from deconvolution is shown at the bottom right. It can be seen that in the absence of noise, the traditional RLD method can recover some image contours and details, but the effect is significantly weaker than that of the CAO-SBD method. In the presence of noise, when the SNR is 20dB, traditional RLD quickly converges to a noise-dominated solution after a few iterations, with most details obscured by background and noise. In contrast, our blind deconvolution method still exhibits prominent details, sharper edges, and less noise impact, outperforming traditional RLD.

When the noise level is higher, with an SNR of 20dB, traditional RLD is almost completely corrupted by noise, while our proposed CAO-SBD method can still recover high-quality images. Figure 3c shows the deconvolution reconstruction result errors under different PSFs. As the noise level increases, the RMSE error of the traditional RLD method (both with and without noise) rises rapidly, while the CAO-SBD method changes more slowly.

Corresponding to the specific colored lines in Figure 3b, we display their profile in Figure 3d, comparing the detail curves at noise-free and different noise levels. At noise-free conditions, the fluctuation peaks and valleys of the grayscale values in the image restored by the traditional RLD method are only about half of those in blind deconvolution. As the noise level gradually increases, the CAO-SBD method smooths the noise while preserving the edge details of the image, while the traditional RLD algorithm becomes almost invisible. This phenomenon directly proves the robustness of our CAO-SBD method to noise.

3.2. Cao-SBD Method for Bovine Pulmonary Artery Endothelial Cells under Wide-Field Fluorescence Microscope

To validate the performance of our CAO-SBD method, we conducted wide-field fluorescence imaging experiments on BPAEC (Invitrogen FluoCells Prepared Slide #1). The mitochondria in the live cells were stained by MitoTracker Red CMXRos, a dye whose accumulation is dependent on the membrane potential. After the cells were fixed and made permeable, F-actin was labeled using Alexa Fluor 488 phalloidin, and the nuclei were counterstained with the blue-fluorescent DNA stain DAPI. For wide-field fluorescent imaging, an inverted fluorescence microscope (Zeiss Observer Z1), equipped with a 40×/0.6NA objective lens, and a cooled sCMOS camera (PCO GmbH, PCO.edge 4.2, 2048 × 2048 pixel resolution, 6.5μm pixel size) located at the native image plane. The central wavelengths of fluorescent emission are 520 and 598nm, respectively. Our experimental results, as shown in **Figure 4**, successfully validated the effectiveness of the CAO-SBD method.

Figure 4a displays the original image of F-actin labeled with AF488 Phalloidin, along with the reconstruction results from the traditional RLD method and our CAO-SBD method. The bottom right corner shows the pupil aberration corrected by the CAO-SBD method. We enlarged the regions of interest (ROI) in the original image of Figure 4a to compare the original image with the reconstruction results from the two methods. It can be visually observed that, in different regions, the original images captured by wide-field fluorescence are relatively blurred. While the traditional RLD algorithm can recover some image details but is sensitive to background noise, our method, which combines sparse priors and Zernike constraints, can display clearer and more detailed images. This is particularly evident in the profile plots from Figures 4c1–c3, which show the profiles at different line positions in the enlarged images. It can be seen that, due to inevitable noise and aberration interference in the experiment, the PSF of the traditional RLD method is distorted, leading to a certain deviation between the theoretical and actual values of the PSF, which affects the deconvolution reconstruction results. The proposed CAO-SBD method can recover high-quality images with only a single raw image, significantly improving the imaging clarity and contrast of F-actin in BPAEC.

To further validate the above conclusions, we also conducted experiments on mitochondria labeled with MitoTracker Red CMXRos. The reconstruction effects are shown in Figure 4d, with the bottom right corner displaying the pupil aberration (which is the same as the F-actin channel). Figures 4e1–e3 show the mitochondrial structures in different ROIs of Figure 4d, from left to right, displaying the original blurred image, the reconstruction result using the traditional RLD method, and the reconstruction result using our method. It can be visually observed that, in different areas, due to PSF distortion and noise interference, the image reconstruction results of the traditional RLD method are not ideal, with a large amount of detailed information being obscured by the background and noise, severely reducing imaging resolution. Processing the same set of original images with the CAO-SBD method, which combines sparse priors and Zernike constraints, can well correct aberrations and suppress noise, obtaining higher quality image reconstruction results than the traditional RLD method, and clearly displaying the mitochondrial morphology. In Figures 4f1–f3, the profile plots at different line positions in the enlarged mitochondrial ROIs are shown. It can be seen that the original images of mitochondria and the reconstruction results under the traditional RLD method have lost detailed information, resulting in flat pixel curve changes. Consistent with the simulation results, in the presence of possible aberrations and noise, the CAO-SBD method always shows better results than the traditional RLD method. The pixel values of the details exhibit pronounced peak and valley features, revealing a distinct mitochondrial morphology. This clarity is crucial for the investigation of mitochondrial dynamics. We present the imaging results more intuitively in Video S1 (Supporting Information).

3.3. CAO-SBD Method for Bovine Pulmonary Artery Endothelial Cells under Confocal Laser Scanning Microscope

In the previous section, we imaged BPAEC using a wide-field fluorescence microscope, successfully validating the effectiveness of the CAO-SBD method. To further demonstrate the universality and applicability of the CAO-SBD method, in this section, the difficulties are particularly amplified when it comes to confocal microscopy. The light intensity captured is considerably weaker than that in wide-field microscopy, which poses a challenge in achieving an optimal SNR. Using theoretically derived PSF for routine applications is impractical, as there is often a considerable divergence between the theoretical PSF and what is actually measured.

© 2025 Wiley-VCH GmbH

18638899, 0, Downloaded from https://onlinelibrary.wiley.com/doi/10.1002/lpor.202500032 by Nanjing University Of Science, Wiley Online Library on [09/05/2025]. See the Terms and Conditions (https://onlinelibrary.wiley.com/terms-and-conditions) on Wiley Online Library for rules of use; OA articles are governed by the applicable Creative Commons License

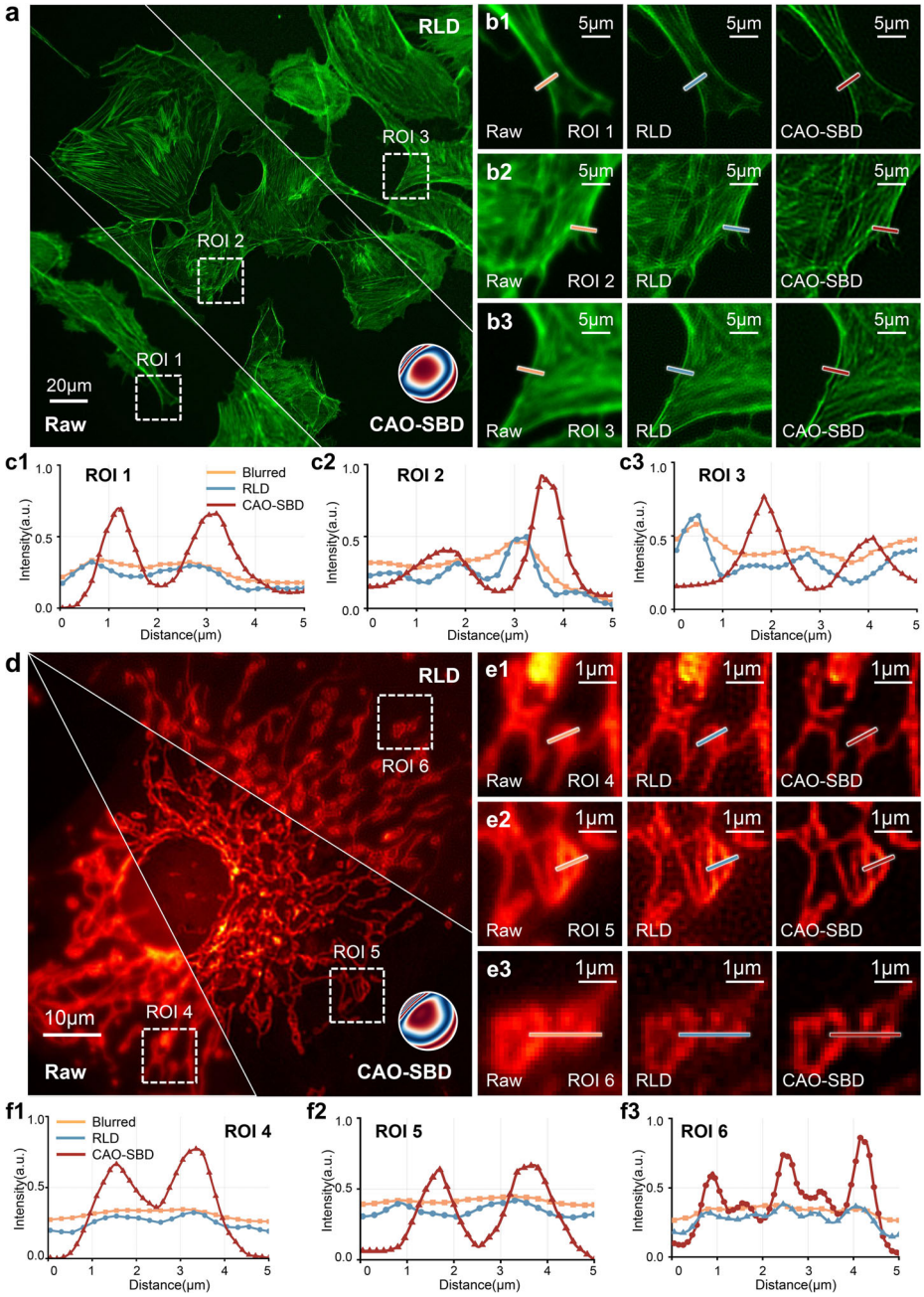

Figure 4. Wide-field fluorescence experiment results of BPAEC. a) Raw image and reconstruction results of F-actin. Scale bar: 20μm. b1–b3) Enlarged regions in a), showing the raw image and the reconstruction results from the traditional RLD method and CAO-SBD. Scale bar: 5μm. c1–c3) Profiles of different colored lines in (b1-b3). d) Raw image and reconstruction results of mitochondria. Scale bar: 10μm. e1-e3) Enlarged regions in (d), showing the raw image and the reconstruction results from the traditional RLD method and CAO-SBD. Scale bar: 1μm. f1-f3) Profiles of different colored lines in (e1-e3) (see Video S1, Supporting Information).

We used a confocal laser scanning microscope (Olympus FV3000) equipped with a 100×/1.45NA oil immersion objective lens (Olympus) to image the BPAEC. The experimental results are detailed in **Figure 5**. The fluorescence triple channels are F-actin (green), mitochondria (red), and cell nuclei (blue), respectively. Figure 5 compares confocal observations and deconvolution reconstruction results from different methods. In Figures 5b1–b3, we focus on the mitochondrial structures of the cells within the ROIs of Figure 5a. Despite their superior sharpness compared to standard epifluorescence images, confocal microscopy images still suffer from degradation caused by residual out-of-focus light and noise associated with photon-limited detection. The system is designed to collect only photons that pass through the pinhole, which results in a substantial amount of noise in the raw data. This inherent noise often restricts the utility of the traditional RLD method, particularly when attempting to

© 2025 Wiley-VCH GmbH

18638899, 0, Downloaded from https://onlinelibrary.wiley.com/doi/10.1002/lpor.202500032 by Nanjing University Of Science, Wiley Online Library on [09/05/2025]. See the Terms and Conditions (https://onlinelibrary.wiley.com/terms-and-conditions) on Wiley Online Library for rules of use; OA articles are governed by the applicable Creative Commons License

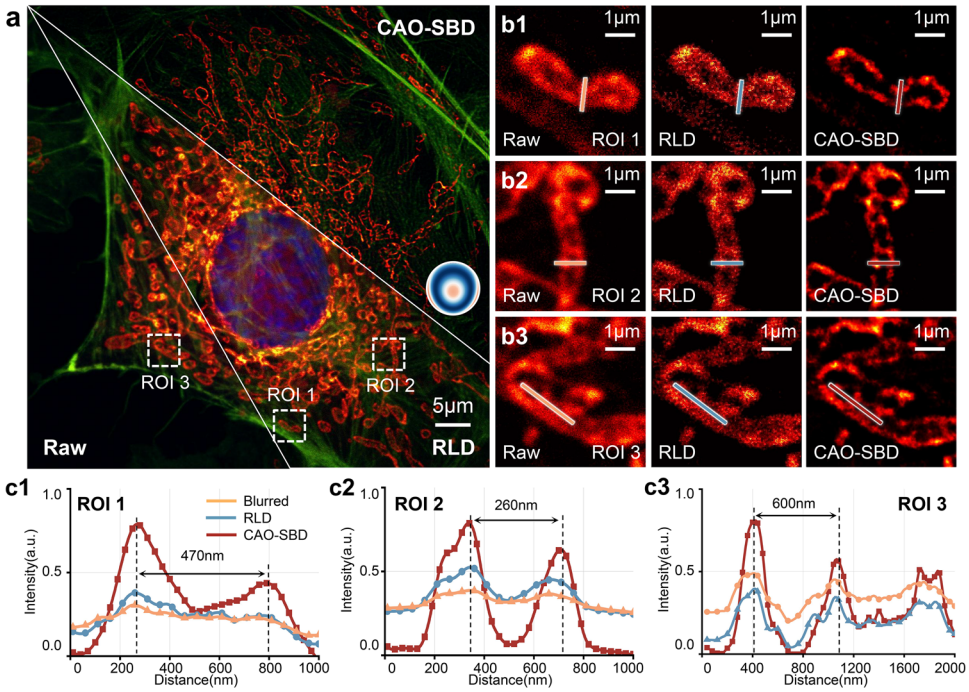

Figure 5. Experimental results of multi-labeled BPAEC under confocal laser scanning microscope. a) Multi-channel fluorescence merge results, including F-actin (green), mitochondria (red), and cell nuclei (blue). Comparisons of raw images with deconvolution reconstruction results. Scale bar: 5μm. b1-b3) Enlarged details of the mitochondrial structures within the marked rectangular area in (a), highlight the characteristics of mitochondrial structures in different regions. Scale bar: 1μm. c1-c3) Profiles of different colored lines in b1-b3) (see Video S2, Supporting Information).

resolve high-resolution structures. In contrast, the CAO-SBD effectively suppresses noise and significantly improves image resolution. As shown in Figures 5c1–c3, they display the profiles of different colored lines in Figures 5b1–b3. It is evident from the figures that the CAO-SBD method more clearly highlights the fine structures of the cristae within mitochondria compared to the traditional RLD method. The minimum center-to-center distance of the line contours shows a conservatively estimated resolution of 260 nm and effectively suppresses noise, resulting in smoother pixel value curves. Our method has demonstrated superior performance over traditional RLD methods across various imaging systems, showcasing its broad applicability We present the imaging results more intuitively in Video S2 (Supporting Information). We also did other supplemental experiments under the confocal laser scanning microscope, and the experimental results are shown in Section S5 and Video S3 (Supporting Information). This achievement not only validates the effectiveness of our approach but also, given the significant role of mitochondrial research in modern biomedicine and its potential applications, our method holds substantial promise in advancing the development of therapeutic strategies for mitochondrial-related diseases and biomedical research.

4. Conclusion and Discussion

In this work, we have successfully developed and validated a novel blind deconvolution method, termed CAO-SBD, which integrates sparse priors with Zernike constraints to correct for aberrations and enhance the resolution of imaging, demonstrating significant efficacy in enhancing imaging quality for two prevalent fluorescence microscopes: wide-field fluorescent microscope and confocal laser scanning microscope. If the sample does not meet the sparse condition, the estimate may produce some error(see Section S4, Supporting Information). Our approach has demonstrated superior performance over the conventional widely used RLD method. By estimating both the PSF and the original object from a single blurred observation, our method bypasses the need for precise PSF determination, which is often challenging in complex imaging systems. Notably, the computational efficiency of our framework has been substantially optimized through CUDA-based parallelization, achieving a 25× acceleration in PSF estimation compared to conventional implementations (see Section S6, Supporting Information for detail).

The integration of sparsity priors and Zernike polynomials not only stabilizes the deconvolution process but also enhances the robustness against noise sensitivity. The experimental results on BPAEC have validated the effectiveness of our method, revealing that it is promising for biological research, such as in-depth investigations of cellular functions and disease mechanisms.

In the end, there remain several important issues that necessitate clarification or further investigation. First, wide-field and confocal microscopes are the most commonly used types of microscope systems in practical applications. However, many other, more novel types of microscopes, such as the two-photon confocal microscope,[56] 4Pi microscope,[57] and other super-resolution imaging systems,[58,59] yield better performance than the ones described earlier. The CAO-SBD method that we present in this paper may further explore its potential in such advanced microscopy techniques. Second, for real-time imaging applications, it's unavoidable to encounter spatial non-uniformity and tempo-

© 2025 Wiley-VCH GmbH

18638899, 0, Downloaded from https://onlinelibrary.wiley.com/doi/10.1002/lpor.202500032 by Nanjing University Of Science, Wiley Online Library on [09/05/2025]. See the Terms and Conditions (https://onlinelibrary.wiley.com/terms-and-conditions) on Wiley Online Library for rules of use; OA articles are governed by the applicable Creative Commons License

rally varying system aberrations due to factors such as the optically inhomogeneous structure of biological specimens, mechanical instability of the microscope, and thermal fluctuations in the environment.[60] The computational acceleration achieved in this work (e.g., completing 50 iterations of RL deconvolution on a 2048 × 2048 image in merely 24.9 s, representing a 39× speedup)establishes a critical foundation toward real-time processing capabilities, and the CAO-SBD method, which estimates aberrations from a single image, shows promise and is well-suited for long-term observation. Third, while the CAO-SBD method presented in this paper is currently confined to 2D image deconvolution, it is recognized that 3D image deconvolution methods are particularly important for the study of thick biological specimens. Expanding the CAO-SBD method to 3D imaging deconvolution presents a highly valuable direction for future research. Finally, the CAO-SBD method presented in this paper is based on incoherent fluorescent imaging. Exploring ways to extend the method into partially coherent imaging,[61,62] such as phase imaging and optical diffraction tomography,[1,63–65] is also of significant importance.

Supporting Information

Supporting Information is available from the Wiley Online Library or from the author.

Acknowledgements

R.-Z., H.-D., and N.-Z. contributed equally to this work. This work was supported by the National Natural Science Foundation of China (62227818, 62105151, 62175109, U21B2033, 62275125, 62275121, 12204239, and 62175109), Leading Technology of Jiangsu Basic Research Plan (BK20192003), Biomedical Competition Foundation of Jiangsu Province (BE2022847), Key National Industrial Technology Cooperation Foundation of Jiangsu Province (BZ2022039).

Conflict of Interest

The authors declare no conflict of interest.

Data Availability Statement

The data that support the findings of this study are available from the corresponding author upon reasonable request.

Keywords

adaptive optics, blind deconvolution, sparsity prior

Received: January 6, 2025
Revised: February 28, 2025
Published online:

[1] C. Zuo, J. Li, J. Sun, Y. Fan, J. Zhang, L. Lu, R. Zhang, B. Wang, L. Huang, Q. Chen, *Opt. Lasers Eng.* **2020**, *135*, 106187.
[2] W. Yang, R. Yuste, *Nat. Methods* **2017**, *14*, 349.
[3] S. F. Gibson, F. Lanni, *JOSA A* **1991**, *8*, 1601.
[4] M. J. Booth, *Light: Sci. Appl.* **2014**, *3*, e165.
[5] N. Ji, *Nat. Methods* **2017**, *14*, 374.
[6] K. M. Hampson, R. Turcotte, D. T. Miller, K. Kurokawa, J. R. Males, N. Ji, M. J. Booth, *Nat. Rev. Methods Primers* **2021**, *1*, 68.
[7] B. Seong, W. Kim, Y. Kim, K.-A. Hyun, H.-I. Jung, J.-S. Lee, J. Yoo, C. Joo, *Light: Sci. Appl.* **2023**, *12*, 269.
[8] M. Ranathunga, J. Kim, T. Moon, S. Song, J. J. Kim, J.-K. Choi, J. Song, C. Joo, *Laser Photonics Rev.* **2025**, *19*, 2401544.
[9] N. Ji, D. E. Milkie, E. Betzig, *Nat. Methods* **2010**, *7*, 141.
[10] E. E. Diel, J. W. Lichtman, D. S. Richardson, *Nat. Protoc.* **2020**, *15*, 2773.
[11] T. Furieri, D. Ancora, G. Calisesi, S. Morara, A. Bassi, S. Bonora, *Biomed. Opt. Express* **2021**, *13*, 262.
[12] L. Hu, L. Xuan, Y. Liu, Z. Cao, D. Li, Q. Mu, *Opt. Express* **2004**, *12*, 6403.
[13] I. N. Papadopoulos, J.-S. Jouhanneau, J. F. Poulet, B. Judkewitz, *Nat. Photonics* **2017**, *11*, 116.
[14] J. M. Beckers, *In: Annual rev. astronomy astrophys. (A94-12726 02-90)* **1993**, *31*, 13.
[15] F. Roddier,*Adaptive Optics in Astronomy*, Cambridge University Press, Cambridge**1999**.
[16] D. L. Fried, *JOSA* **1982**, *72*, 52.
[17] R. W. Wilson, *Mon. Not. R. Astron. Soc.* **2002**, *337*, 103.
[18] R. V. Shack, in *Spring Meeting of Optical Society of America, 1971*, vol. *656*, Optica Publishing Group, Washington, DC **1971**.
[19] B. C. Platt, R. Shack, *J. Refract. Surg.* **2001**, *17*, S573.
[20] B. Stoklasa, L. Motka, J. Rehacek, Z. Hradil, L. Sánchez-Soto, *Nat. Commun.* **2014**, *5*, 3275.
[21] T. Wu, M. Guillon, G. Tessier, P. Berto, *Optica* **2024**, *11*, 297.
[22] G.-H. Go, D.-g. Lee, J. Oh, G. Song, D. Lee, M. Jang, *Light: Sci. Appl.* **2024**, *13*, 187.
[23] Z. Qin, Z. She, C. Chen, W. Wu, J. K. Lau, N. Y. Ip, J. Y. Qu, *Nat. Biotechnol.* **2022**, *40*, 1663.
[24] Z. Zhou, J. Huang, X. Li, X. Gao, Z. Chen, Z. Jiao, Z. Zhang, Q. Luo, L. Fu, *PhotoniX* **2022**, *3*, 13.
[25] C. He, J. Antonello, M. J. Booth, *eLight* **2023**, *3*, 23.
[26] R. Ng, P. M. Hanrahan, in *International Optical Design Conference*, Optica Publishing Group, Washington, DC **2006**, p. WB2.
[27] M. Levoy, R. Ng, A. Adams, M. Footer, M. Horowitz, in *Acm Siggraph 2006 papers*, ACM, New York **2006**, pp. 924–934.
[28] M. Levoy, Z. Zhang, I. McDowall, *J. Microsc.* **2009**, *235*, 144.
[29] I. Ihrke, J. Restrepo, L. Mignard-Debise, *IEEE Signal Process. Mag.* **2016**, *33*, 59.
[30] J. Wu, Z. Lu, D. Jiang, Y. Guo, H. Qiao, Y. Zhang, T. Zhu, Y. Cai, X. Zhang, K. Zhanghao, H. Xie, T. Yan, G. Zhang, X. Li, Z. Jiang, X. Lin, L. Fang, B. Zhou, P. Xi, J. Fan, L. Yu, Q. Dai, *Cell* **2021**, *184*, 3318.
[31] J. Wu, Y. Guo, C. Deng, A. Zhang, H. Qiao, Z. Lu, J. Xie, L. Fang, Q. Dai, *Nature* **2022**, *612*, 62.
[32] R. W. Gerchberg, *Optik* **1972**, *35*, 237.
[33] M. Chen, Z. F. Phillips, L. Waller, *Opt. Express* **2018**, *26*, 32888.
[34] G. Zheng, X. Ou, R. Horstmeyer, C. Yang, *Opt. Express* **2013**, *21*, 15131.
[35] P. Song, S. Jiang, H. Zhang, X. Huang, Y. Zhang, G. Zheng, *APL Photonics* **2019**, *4*, 5.
[36] C. Zuo, Q. Chen, W. Qu, A. Asundi, *Opt. Lett.* **2013**, *38*, 1724.
[37] Y. Shu, J. Sun, J. Lyu, Y. Fan, N. Zhou, R. Ye, G. Zheng, Q. Chen, C. Zuo, *PhotoniX* **2022**, *3*, 24.
[38] N. Zhou, R. Zhang, R. Zhu, Z. Zhou, H. Wu, Q. Chen, P. Gao, J. Sun, C. Zuo, *Laser Photonics Rev.* **2025**, 2402196.
[39] T. J. Holmes, *JOSA A* **1992**, *9*, 1052.

© 2025 Wiley-VCH GmbH

18638899, 0, Downloaded from https://onlinelibrary.wiley.com/doi/10.1002/lpor.202500032 by Nanjing University Of Science, Wiley Online Library on [09/05/2025]. See the Terms and Conditions (https://onlinelibrary.wiley.com/terms-and-conditions) on Wiley Online Library for rules of use; OA articles are governed by the applicable Creative Commons License

[40] T. J. Holmes, S. Bhattacharyya, J. A. Cooper, D. Hanzel, V. Krishnamurthi, W.-c. Lin, B. Roysam, D. H. Szarowski, J. N. Turner, *Handbook Biology Confocal Microscopy* Springer US, Boston, MA, **1995**.
[41] W. Denk, D. Piston, W. Webb, *Two-photon molecular excitation in laser-scanning microscopy*, 2nd edn., Plenum Press, New York **1995**, pp. 445–458.
[42] V. Krishnamurthi, Y.-H. Liu, S. Bhattacharyya, J. N. Turner, T. J. Holmes, *Appl. Opt.* **1995**, *34*, 6633.
[43] A. Levin, Y. Weiss, F. Durand, W. T. Freeman, in *2009 IEEE conference on computer vision and pattern recognition*, IEEE, Piscataway, NJ **2009**, pp. 1964–1971.
[44] D. S. Biggs, *Curr. Protoc. Cytom.* **2010**, *52*, 12.
[45] R. Zhang, N. Zhou, H. Tang, M. Xia, Z. Cai, J. Sun, Q. Chen, C. Zuo, *Laser Photonics Rev.* **2024**, *18*, 2300770.
[46] J. W. Goodman, *Introduction to Fourier optics*, Roberts and Company publishers, Boston **2005**.
[47] L. B. Lucy, *Astron. J.* **1974**, *79*, 745.
[48] W. H. Richardson, *JOSA* **1972**, *62*, 55.
[49] H. Engl, M. Hanke, A. Neubauer, *Regularization of Inverse Problems, Springer Science & Business Media*,**1996**, *375*.
[50] W. Zhao, S. Zhao, L. Li, X. Huang, S. Xing, Y. Zhang, G. Qiu, Z. Han, Y. Shang, D.-e. Sun, C. Shan, R. Wu, L. Gu, S. Zhang, R. Chen, J. Xiao, Y. Mo, J. Wang, W. Ji, X. Chen, B. Ding, Y. Liu, H. Mao, B.-L. Song, J. Tan, J. Liu, H. Li, L. Chen, *Nat. Biotechnol.* **2022**, *40*, 606.
[51] J. Wang, D. E. Silva, *Appl. Opt.* **1980**, *19*, 1510.
[52] M. Born, E. Wolf, *Principles of optics: electromagnetic theory of propagation, interference and diffraction of light*, Elsevier, Amsterdam **2013**.
[53] G. B. Airy, *Trans. Cambridge Phil. Soc.* **1835**, *5*, 283.
[54] R. C. Gonzalez, *Digital image processing*, Pearson education india, **2009**.
[55] Y. Hiraoka, J. W. Sedat, D. A. Agard, *Biophys. J.* **1990**, *57*, 325.
[56] A. Diaspro, *Confocal and two-photon microscopy: foundations, applications and advances*, John Wiley & Sons, New York **2001**.
[57] S. Hell, E. H. K. Stelzer, *JOSA A* **1992**, *9*, 2159.
[58] J. Qian, Y. Cao, Y. Bi, H. Wu, Y. Liu, Q. Chen, C. Zuo, *eLight* **2023**, *3*, 4.
[59] C. Zhang, B. Yu, F. Lin, S. Samanta, H. Yu, W. Zhang, Y. Jing, C. Shang, D. Lin, K. Si, W. Gong, J. Qu, *PhotoniX* **2023**, *4*, 38.
[60] S. Skylaki, O. Hilsenbeck, T. Schroeder, *Nat. Biotechnol.* **2016**, *34*, 1137.
[61] N. Zhou, J. Sun, R. Zhang, R. Ye, J. Li, Z. Bai, S. Zhou, Q. Chen, C. Zuo, *ACS Photonics* **2023**, *10*, 2461.
[62] N. Zhou, R. Zhang, W. Xu, R. Zhu, H. Tang, X. Zhou, J. Sun, P. Gao, Q. Chen, C. Zuo, *Laser Photonics Rev.* **2024**, *18*, 2400387.
[63] C. Zuo, Q. Chen, W. Qu, A. Asundi, *Opt. Express* **2013**, *21*, 24060.
[64] C. Zuo, J. Sun, J. Li, J. Zhang, A. Asundi, Q. Chen, *Sci. Rep.* **2017**, *7*, 7654.
[65] C. Zuo, J. Sun, J. Li, A. Asundi, Q. Chen, *Opt. Lasers Eng.* **2020**, *128*, 106003.

© 2025 Wiley-VCH GmbH

18638899, 0, Downloaded from https://onlinelibrary.wiley.com/doi/10.1002/lpor.202500032 by Nanjing University Of Science, Wiley Online Library on [09/05/2025]. See the Terms and Conditions (https://onlinelibrary.wiley.com/terms-and-conditions) on Wiley Online Library for rules of use; OA articles are governed by the applicable Creative Commons License